IEEE Photonics Journal
An IEEE Photonics Society Publication

Polarization Splitting Grating Coupler for Optical Antenna of LiDARs Consisting of Two Gratings Coupling Light in a Perfectly Vertical Direction

Volume 13, Number 3, June 2021

Tetsuya Shimogaki
Hikaru Fukushima
Daisuke Inoue
Tadashi Ichikawa
Tatsuya Yamashita

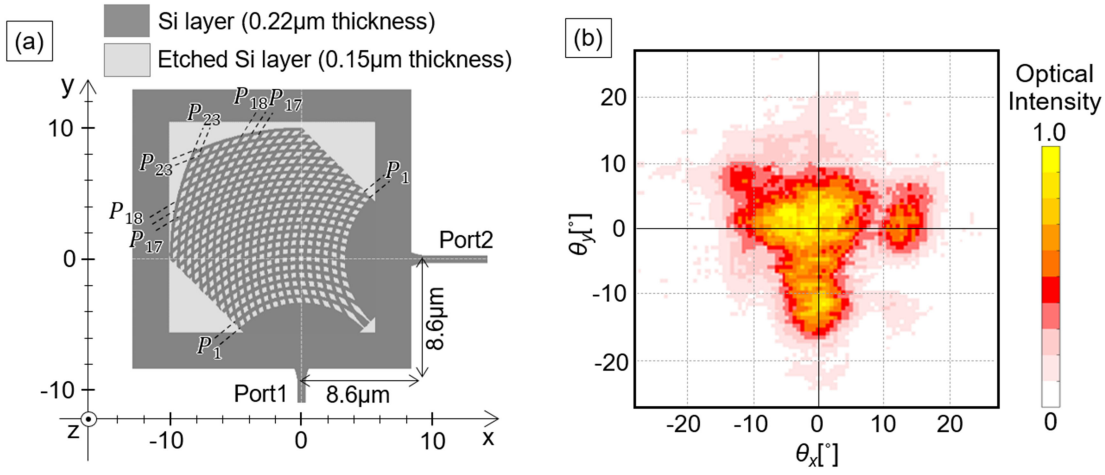

DOI: 10.1109/JPHOT.2021.3079933

Polarization Splitting Grating Coupler for Optical Antenna of LiDARs Consisting of Two Gratings Coupling Light in a Perfectly Vertical Direction

Tetsuya Shimogaki,[1] **Hikaru Fukushima**,[1] **Daisuke Inoue**,[1] **Tadashi Ichikawa**,[1] **and Tatsuya Yamashita**[1]

[1]Toyota Central R&D Labs., Inc., Aichi 480-1192, Japan

DOI:10.1109/JPHOT.2021.3079933

Manuscript received January 21, 2021; revised April 28, 2021; accepted May 10, 2021. Date of publication May 13, 2021; date of current version May 28, 2021. Corresponding author: Tetsuya Shimogaki (e-mail: shimogaki@mosk.tytlabs.co.jp).

Abstract: Grating couplers (GCs) are devices for transmitting and receiving the light propagated in a waveguide in silicon photonic integrated circuits (PICs). In this study, we propose a polarization splitting GC (PSGC) for the optical antenna of light detection and ranging (LiDAR). The PSGC was designed on the basis of two GCs coupling in a perfectly vertical direction. Our experiment demonstrated that the designed PSGC transmitted a polarization-multiplexed beam. The transmitting and receiving efficiencies of the optical antenna consists of lenses and PSGCs were calculated, and then the optical parameter for maximizing them was clarified.

Index Terms: Silicon nanophotonics, Sensors.

1. Introduction

Light detection and ranging (LiDAR) is one of the most attractive long-range three-dimensional (3D) imaging sensors. LiDAR has a more precise azimuth resolution than RADAR because of the small beam divergence of the laser [1]. Owing to this high resolution, LiDAR sensors have gained popularity in the field of autonomous vehicles and robotics.

Commercially available LiDARs, at present, have some problems in terms of size, cost, and durability. The most dominant cause is a mechanical scanner. Accordingly, many studies have focused on replacing the mechanical scanner with a solid-state scanner. The silicon photonic integrated circuit (PIC) is one of the approaches [2]–[4]. PICs, which use silicon-on-insulator (SOI) platforms, are one of the most promising technologies for dense integration of optical and electrical functions. PICs are expected to be at the technical core of the solid-state compact LiDAR. For example, a non-mechanical scanner with an optical phased array on the PIC chip has been demonstrated by some groups [2], [3]. In addition, optical switching using ring resonators was demonstrated in our previous study [4]. In both cases, grating couplers (GCs), which are fabricated by partial etching on a silicon waveguide, have been utilized as optical transmitters and receivers. Optical transmitters and receivers can be rephrased as the “optical antenna” of PIC-based LiDAR.

GCs couple the light, which propagates in the PIC’s waveguide, with the out-of-plane. Design of GCs has been studied actively, and the coupling loss has improved to be less than 3 dB, which was

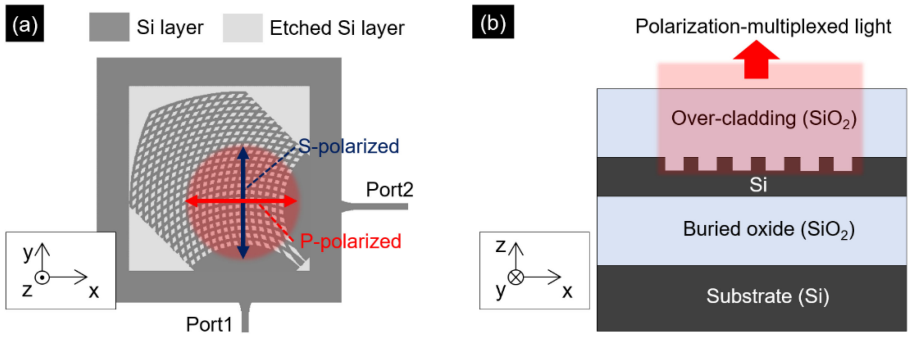

Fig. 1. Schematic view of the proposed PSGC, (a) Top-view (b) Cross-sectional view.

achieved by the optimization of the etching depth, etching pitch, etching width, thickness of each layer, and so on [5]–[9]. Compact GCs have been achieved with the focusing configuration [10]. These optimizations have been intended for application to couple light between fibers and PICs. The optical antenna of LiDARs is a relatively new application of GCs.

Considering the application of GCs in the optical antenna of the LiDAR, their polarization-dependent loss affects the detection sensitivity. Polarization-insensitive GCs with single waveguide port have been reported for the purpose of fibers to chip coupling [11]. In this case, P- and S-polarized light from the fiber have coupled to the waveguide thorough GCs. However, the polarization-insensitive GCs were fabricated on a non-standard SOI wafer with a 340 nm thick top silicon layer in order to propagate TE and TM modes. For a LiDAR application, it is necessary to insert couplers which separate or combine TE and TM modes before general optical components (e.g., Multimode interference couplers). It leads to being undesired complexing system and excess optical losses. Another approach to the polarization-insensitive GCs is the splitting the two orthogonal polarizations in two opposite directions. Zaoui reported a simple scheme of the splitting GCs on a standard SOI with a 220 nm thick of top silicon layer [12]. This structure has different TE and TM hot spots, which are 10 μm apart from each other. Accordingly, in the case of LiDAR application, the transmitted light from their proposed GCs would be divided clearly two different beams. The polarization dependent loss would not be improved. Furthermore, the both polarization-insensitive GCs occupy a large area since they have long taper structures. This leads to a growing chip cost.

There have been some reports that polarization splitting grating couplers (PSGCs) with two-dimensional (2D) structures achieved low polarization dependent losses [13]–[15]. PSGCs have 2D etched slots on a 220 nm thick of top silicon layer. Waveguide ports are connected orthogonally, and split polarizations couple to each port. A well-designed PSGC can couple the two orthogonal polarized lights in the direction along the same beam axis in free space. They reported that compact 2D PSGCs achieved high coupling efficiency and low polarization-dependent loss in fiber-chip coupling. Therefore, we have been trying to improve the PIC-based LiDAR's optical antenna to be polarization-independent by utilizing PSGCs.

In this study, we demonstrated PSGCs designed for optical antennas of LiDAR on a 220 nm SOI platform with the ordinal etching process, which is available in multi-project wafer of general foundries. Fig. 1(a) shows a schematic top view of the designed PSGC. Fig. 1(b) shows a cross-sectional view. It is required that both P- and S-polarized lights are diffracted in the same direction to utilize PSGC for LiDAR. We adopted a straightforward structure in which P- and S-polarized lights are diffracted in the vertical direction with respect to the chip surface. It can be realized with two vertical GCs (VGCs). VGC is defined here as the GC coupling the light in a perfectly vertical direction. Our VGCs have fan-like structures, characterized by small footprint and concentric radiation of diffracted light. The proposed PSGC also has the advantage of low packaging cost because of the ease of alignment owing to the perfectly vertical coupling. Fig. 2

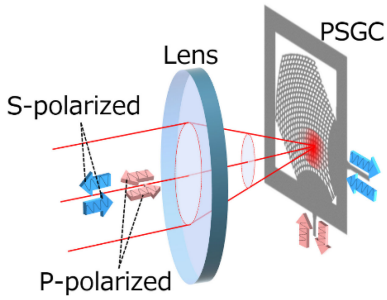

Fig. 2. Example of the optical alignment required for the application of a PSGC to a LiDAR antenna.

shows an example of the optical alignment required for the application of PSGC's to a LiDAR antenna. In this example, the P- and S-polarized lights are collimated with the lens and then they are transmitted and received.

In the first half of this paper, the simulation results of the designed VGC's output lights and the evaluated results of the fabricated VGCs are reported. The designed VGCs exhibit an improvement in the diffraction efficiency without any metal reflection mirrors or any other post-processing. The PSGC was designed by a slight modification of VGCs to match the near field patterns (NFPs) of the P- and S-polarized lights. The simulation and evaluated results of the PSGC are reported in the last half of this paper. The emitting and receiving efficiencies of the PIC-based LiDAR utilizing fabricated PSGCs were also calculated, and then the optics parameter for maximizing them was clarified.

2. VGC

2.1 Design and Simulation

The diffraction angle of the GC is determined by the gap in the effective refractive index around the grating teeth. The effective refractive index is adjusted by some parameters, such as pitch (p), the duty ratio of teeth (d), and depth of partial etching (e). The 1st order diffraction angle θ_{GC} can be expressed as:

$$\theta_{GC} = sin^{-1}\left(\frac{n_{eff} - \frac{\lambda}{p}}{n_{clad}}\right) \tag{1}$$

$$n_{eff} = d \cdot n_e + (1 - d) \cdot n_o \tag{2}$$

where n_{eff} is an effective refractive index of the grating section [8]. The wavelength λ is set to be 1.55 μm in this study due to the eye-safe LiDAR application. n_{clad} is the effective index of the clad medium, n_e is that of the etched trench and n_o is of the unetched tooth. VGC's design parameters can be roughly estimated from these equations. However, in principle, the diffracted light reduces drastically in the case of perfectly vertical coupling because of the significant second-order Bragg's reflection.

The improvement of the coupling efficiency of VGCs were achieved in some reports by non-periodic structures which have chirped structures [16]–[19]. Well-designed chirped structure can reduce the reflection, which improves the coupling efficiency of VGCs. Fig. 3(a) shows a schematic of the VGC designed in this study. It is a simple and fabrication-tolerant method to improve the diffraction efficiency of VGCs because it does not require any post-processing or additional reflector layers.

The VGC is designed for an SOI wafer with a 220 nm silicon layer deposited on a 3 μm buried oxide layer and 3 μm over-cladding. The buried oxide and over-cladding consist of silicon dioxide. The waveguide for single TE mode with a width of 500 nm is connected to an exponential taper with a width of the end is 0.84 μm. The taper is connected to a fan-like structure. The taper

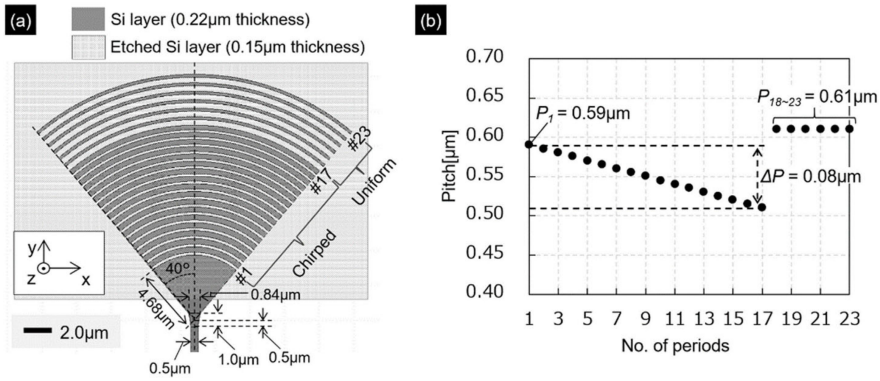

Fig. 3. Designed VGC, (a) Top view of the VGC's silicon layer (b) Pitches at individual periods ($P_1 = 0.59\ \mu$m).

was designed to reduce the mode-conversion loss. The grating grooves are formed on a fan-like structure. Concentric arcs, which have the same center point as that of the fan-like structure, were formed by partial etching of the silicon layer. The distance from the center point to the concentric arcs is set to 4.68 μm. The center point of them are 0.5 μm inside of the end of the exponential taper. The depth of the partial etching was determined at 70 nm due to the foundry restriction. The arcs diffract spreading light with the same phase because the shape of the wavefront matches with that of the arcs. The interior angle of the fan-like structure is 80°.

As shown in Fig. 3(a), the VGC has a chirped section and a uniform section. The diffracted light was simulated using the 3D finite-difference time-domain method (FDTD). The parameters were adjusted to maximize the upward(z-axis) diffraction efficiency. The chirped section ranges from the 1st to the 17th period, and the uniform section ranges from the 18th to the 23rd period. The grating pitches P_i were designed according to following the formula:

$$P_i = \begin{cases} P_1 + \Delta P(i-1)/16 & (1 \le i \le 17) \\ 0.61 & (17 < i \le 23) \end{cases} \tag{3}$$

where i is the number of grating periods. P_i is the pitch width with a unit of a micrometer. Considering the coupling strength, the number of grating periods was designed so that the NFP would fit within the chirped section. The overall number of periods was decided not to exceed 20 μm to maintain compact size. P_1, the first pitch, was varied with a step of 0.01 μm to ensure the tolerance of manufacturing error. ΔP is the difference between P_1 and P_{17}. The duty ratio of the pitch is defined by the slot-pitch ratio. The duty ratio of the chirped section was set to 35%. The duty ratio of the uniform section was set to 65%. These duty ratios and ΔP were determined to meet the manufacturing linewidth. Fig. 3(b) shows the VGC design pitch calculated in the study. In this figure, P_1 is set to be 0.59 μm. The uniform section functions as a reflector that reflects the light transmitted through the chirped section. The pitch of the uniform section $P_{18} - P_{23}$ were determined so that the diffraction efficiency to upward (z-axis direction) would be maximize.

Fig. 4 shows the FDTD results of the designed VGC. Fig. 4(a) shows the NFP in the xy-plane 0.2 μm above the bottom of Si. The optical intensity is the highest for the chirped section. Consequently, most of the incident light is diffracted in the chirped section. The direction of the diffracted light was simulated by far-field patterns (FFPs), as shown in Fig. 4(b). The diffraction angles θ and φ are defined as the spherical coordinates and are shown in the inset of Fig. 4(b). The diffraction efficiency η is defined as the ratio of the total power of the diffracted light in the z-axis direction to the total input power. The direction of diffracted light is the z-axis, that is $\theta = 0°$. The η was 43%, which is a high efficiency attributed to the chirped structure. The η was limited by the bidirectionality of diffracted light.

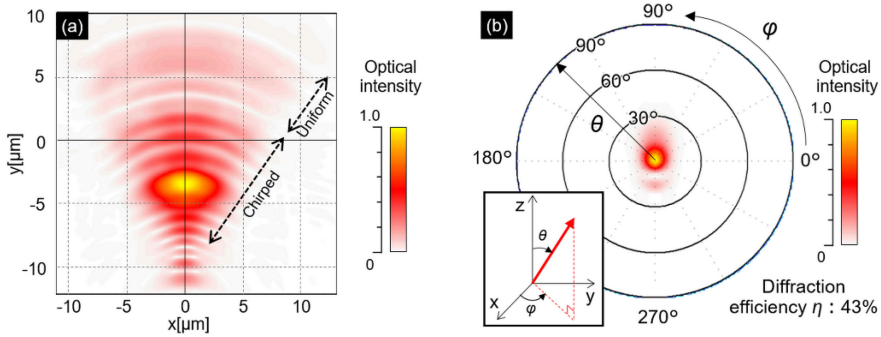

Fig. 4. Simulation results of the diffraction from the VGC, (a) NFP (b) FFP.

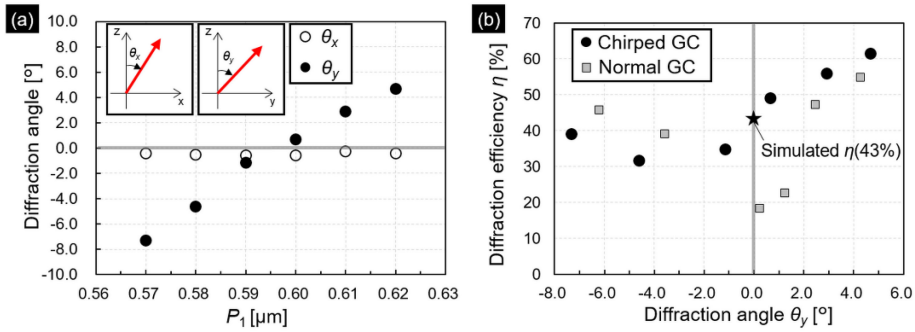

Fig. 5. Measured diffracted light from the designed GCs, (a) Diffraction angles θ_x and θ_y vs P_1 (b) Diffraction efficiency η vs Diffraction angle θ_y.

2.2 Experimental Results

The fabricated GCs were evaluated by exciting the input waveguide with a continuous-wave laser operating at 1.55 μm (Alnair Labs, TLG-200). The diffracted light from the GCs was observed with an optical beam measurement system (SYNERGY OPTOSYSTEMS, M-Scope type S and type F). Fig. 5(a) shows the measured diffraction angle of GCs with P_1 varying from 0.57 μm to 0.59 μm. Plotted data are averaged for three samples. The diffraction angles in the x- and y-directions with respect to the z-axis are defined here as θ_x and θ_y. The relation between θ_x, θ_y, θ, and φ is explained by the following equations:

$$\theta = \cos^{-1}\left(\frac{1}{\sqrt{\tan^2\theta_x + \tan^2\theta_y + 1}}\right) \tag{4}$$

$$\varphi = \tan^{-1}\left(\frac{\tan\theta_y}{\tan\theta_x}\right) \tag{5}$$

θ_x is less than 0.6°, which is assumed to be the alignment error of the measurement system. θ_y approaches 0° when P_1 is around 0.59–0.60 μm.

The characteristics of η as a function of θ_y are shown in Fig. 5(b). As a reference, the characteristics of normal GCs without chirped sections are also plotted in Fig. 5(b). The diffraction efficiency drastically decreased at approximately $\theta_y = 0°$ in the case of normal GCs. On the other hand, the diffraction efficiency of the chirped GCs did not decrease around $\theta_y = 0°$. Considering this tendency and the simulation result of $\eta = 43\%$ at $\theta = 0°$ (plotted in Fig. 5(b) with a star), the diffraction efficiency of the VGC was significantly improved by the chirped structure. Accordingly, the parameters of VGC is determined to be the $P_1 = 0.595$ μm.

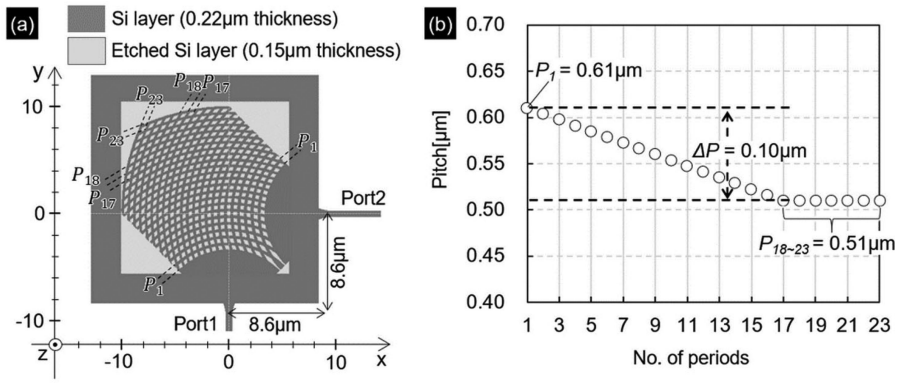

Fig. 6. Design of the PSGC, (a) Top view of the PSGC's silicon layer and (b) Pitches of individual periods.

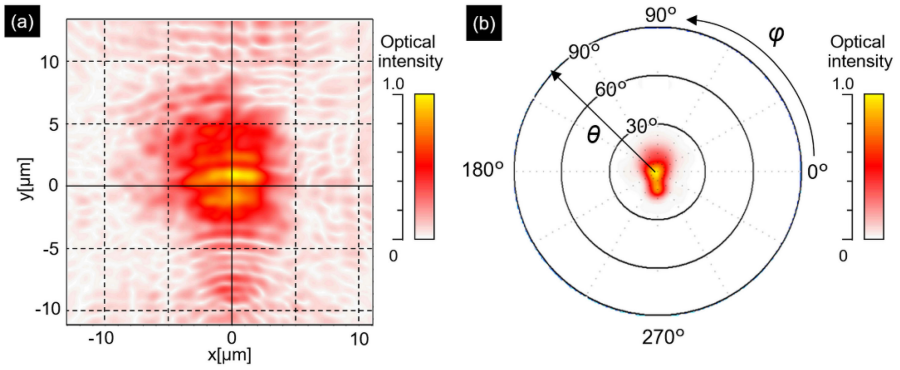

Fig. 7. Simulation results of the diffraction from the designed PSGC (port 1 excited), (a) NFP and (b) FFP.

3. PSGC

3.1 Design and Simulation

We designed the PSGC by merging two VGCs with minor modifications. The initial value of the pitch was adjusted to be larger than that of the VGC. The boundary between the chirped and uniform sections was adjusted to be smooth. Fig. 6(a) shows the top view of the designed PSGC. The PSGC has two input ports 8.6 μm apart. Port 1 aligns with the y-axis direction, and port 2 aligns with the x-axis direction. The design parameters are shown in Fig. 6(b). P_1 and ΔP are slightly modified from those of the VGC because the refractive index is slightly changed due to the crossing grooves. The duty ratio of the chirped and uniform sections is set to 60%. The pitch of the uniform section is designed to be the same as that of P_{18}. These are intended to mitigate the left-right asymmetry caused by two orthogonal VGCs. The interior angle of the fan-like structure is 90°.

Figs. 7 and 8 show the FDTD simulation results of the diffracted light from the designed PSGC, as explained in Fig. 5, also showing the cases of exciting ports 1 and 2, respectively. Figs 7(a) and Fig. 8(a) are NFP images, in which the axes correspond to those of Fig. 6(a). NFP images indicate that most of the lights are diffracted in the same region, around (x, y) = (0, 0), in between periods No. 5-8.

FFP images are shown in Figs. 7(b) and 8(b). Large portion of the light diffracted perfectly in vertical direction in both the FFP images. Protruding shapes with relatively weak intensity were seen in both FFP images. This is due to small portion of light which does not diffract perfectly in vertical direction. The injected light is mainly designed to diffract from period No. 5-8, which is

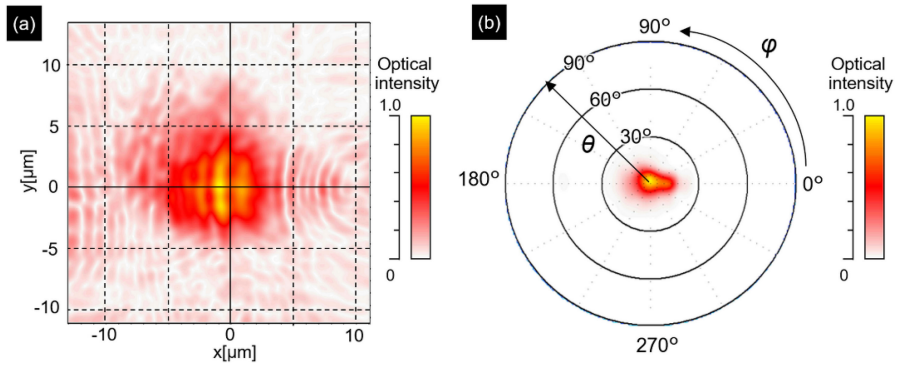

Fig. 8. Simulation results of the diffraction from the designed PSGC (port 2 excited) (a) NFP and (b) FFP.

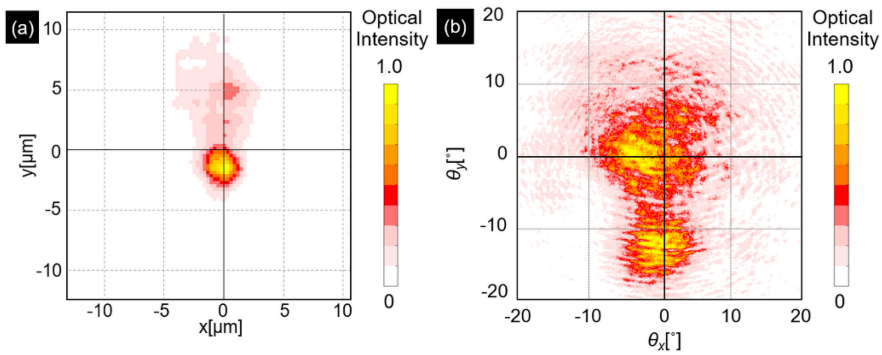

Fig. 9. Experimental results of the diffraction from the designed PSGC (port 1 excited) (a) NFP and (b) FFP.

directed vertically. A small portion of the light propagates through this region and diffracts where the pitches are narrower. This portion corresponds to the light toward tilting to the input port side at the FFP. The diffraction efficiencies η_P and η_S were calculated to be 44% and 43%, respectively.

3.2 Experimental Results

The fabricated PSGCs were evaluated by exciting port 1 and port 2 with the laser. Fig. 9(a) shows an NFP image when port 1 is excited. Fig. 9(b) shows an FFP image when port 1 is excited. The NFP image has the maximum brightness around (x, y) = (0, −1.5), and it was found that a small portion of the light propagates through this region and diffracts.

As shown in Fig. 9(b), there are two diffraction beams. The one diffraction beam, which has a broad divergence angle of approximately 10°, is directed vertically. The other one with a narrower divergence angle is directed such that it is tilted at approximately 12° with respect to $\theta = 0°$. The polarization of the diffracted light was investigated using a polarimeter (Thorlabs, PAX1000). Approximately 98% of the diffracted light was polarized along the x-axis. The remaining 2% was polarized along the y-axis. Accordingly, most of the injected laser maintained its polarization.

Fig. 10(a) and (b) shows the NFP and FFP images when port 2 is excited. Fig. 10 is rotated by 90° with respect to Fig. 9. The diffracted light was measured to be 99% polarized along the y-axis, the remaining 1% was polarized along the x-axis. The diffraction efficiencies (η_P and η_S) were found to be 48% and 46%, respectively, by measuring the total power of the output light.

Therefore, it was confirmed that the input from port 1 can be transmitted as P-polarized light and the input from port 2 as S-polarized light, as intended. The fabricated PSGC does not have ideal performance because the NFPs and FFPs don't have the perfectly same distribution. These

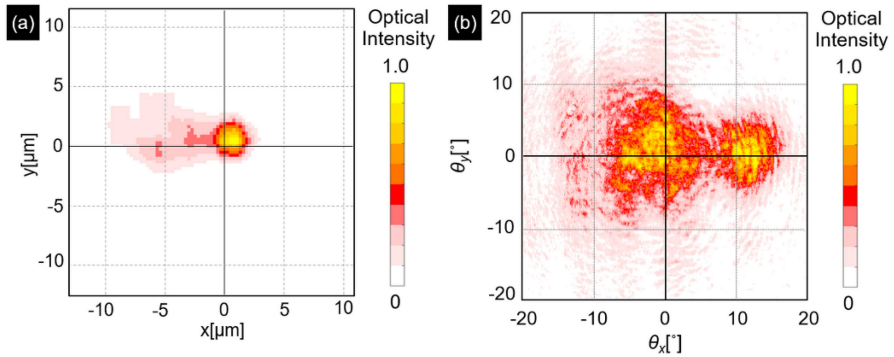

Fig. 10. Experimental results of the diffraction from the designed PSGC (port 2 excited) (a) NFP and (b) FFP.

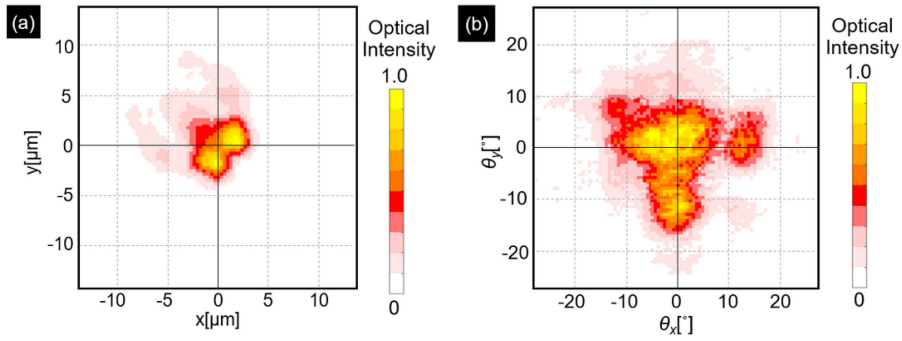

Fig. 11. Experimental results of the diffraction from the designed PSGC (both port 1 and port 2 excited) (a) NFP and (b) FFP.

are assumed to be result of fabrication error. However, the fabricated PSGC has the sufficient possibility as the polarization-multiplexed beam transmitter and receiver.

4. PSGC's Receiving and Transmitting Efficiencies As the Optical Antenna of LiDAR with Lenses

The results shown in section 3.2 indicate that the fabricated PSGC has the functions of a polarization-multiplexed beam transmitter and receiver. To demonstrate their functions, NFP and FFP images were observed with both the ports excited. Fig. 11(a) and (b) shows the measured NFP and FFP images and they are the superposition of Fig. 9 and 10, respectively.

As shown in Fig. 11(a), the NFP is misaligned by several micrometer. This causes a decrease in the receiving efficiency. We have found that the NFP's distribution mismatch could be improved by a slight laser wavelength modulation. Furthermore, a slight (several nano meters) adjust of the P_1 also should be capable to do that. In this section, we only discuss the performance of the fabricated PSGC when it is utilized with a laser of 1.55 μm wavelength. The receiving efficiency was evaluated by separating P- and S-polarized beams (η_{rP} and η_{rS}). When we use the imaging optics for LiDAR reported in our previous paper [4], the receiving efficiency can be calculated by the Airy disk distribution (I_{Airy}) of the lens and the NFP. The Fraunhofer diffraction intensity resulting from the effective aperture diameter D is determined as

$$I_{Airy} = I_0 \left\{ \frac{4J_1\left(\frac{kD}{2}\sin\alpha\right)}{kD\sin\alpha} \right\}^2, \tag{6}$$

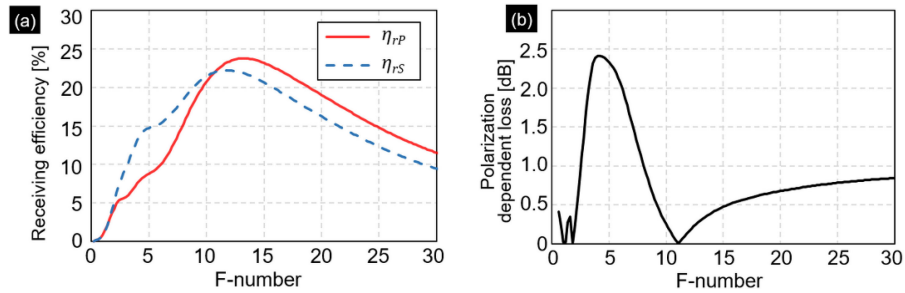

Fig. 12. Relations between the PSGC's receiving performances and f-number (a) Receiving efficiencies of P-polarized and S-polarized light (b) The polarization dependent loss.

where I_0 is the light intensity at the center of the diffraction pattern, and k is the angular wavenumber. In the equation, J_1 is a Bessel function of the first kind. The angle α with respect to the optical axis is calculated by

$$\alpha \simeq \tan^{-1}\left(\frac{\sqrt{(x-x_0)^2+(y-y_0)^2}}{f}\right), \tag{7}$$

where f is the focal length of the lens, and x_0 and y_0 are offsets of the focal point. Using equations (4) and (5), the Airy disk distribution can be calculated for the situation when the received light is focused on the surface of the PSGC. The receiving efficiencies η_{rP} and η_{rS} were calculated as follows:

$$\eta_{rP,rS} = \frac{\iint \left(I_{rP,rS} \cdot I_{Airy}\right) dxdy}{\iint I_{rP,rS} dxdy \cdot \iint I_{Airy} dxdy} \cdot \eta_{P,S} \tag{8}$$

where I_{rP} and I_{rS} are the intensity distributions of Fig. 9(a) and 10(a), respectively. Fig. 12(a) shows the receiving efficiency of the PSGC as a function of f-number with a fixed focal length of 6 mm, as in our previous paper [4]. The (x_0, y_0) was adjusted to be (1.5, -1.5) to get the highest receiving efficiency. The f-number was defined from equation 7.

$$F = \frac{f}{D} \tag{9}$$

The receiving efficiency exhibits a maximum value of approximately 22–24% when the f-number is in the range of 11–;13. There is a slight difference between η_{rP} and η_{rS} because of the misalignment of the NFP shown in Fig. 11(a). Fig. 12(b) shows the polarization-dependent loss as a function of f-number. Polarization-dependent loss is defined here as the absolute value of the difference in coupling losses. The polarization-dependent loss exhibits 0 dB when the f-number is approximately 10.7.

The transmitting efficiencies (η_{tP} and η_{tS}) of the polarization-multiplexed beam were calculated as follows:

$$\eta_{tP,tS} = \frac{\int_0^{\theta_{max}} \int_0^{2\pi} I_{tP,tS} d\varphi d\theta}{\int_0^{\frac{\pi}{2}} \int_0^{2\pi} I_{tP,tS} d\varphi d\theta} \cdot \eta_{P,S} \tag{10}$$

$$\theta_{max} = \tan^{-1}\left(\frac{1}{2F}\right) \tag{11}$$

where I_{tP} and I_{tS} are the intensity distributions of Fig. 9(b) and 10(b), respectively. θ_{max} means the maximal angle of the cone of diffracted light that can enter the lens. Fig. 13(a) shows the relationship between the transmitting efficiencies and the f-number. For the optical receiver to operate at the highest efficiency with the f-number set to 10.7, both η_{tP} and η_{tS} need to be reduced

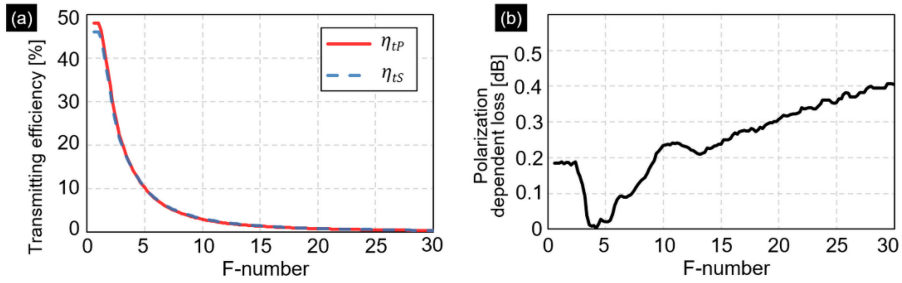

Fig. 13. Relations between the PSGC's transmitting performances and f-number (a) Transmitting efficiencies of P-polarized and S-polarized light (b) The polarization dependent loss.

by approximately 2.5%. In the case where two PSGCs are used to separate the transmitter and receiver, the f-number of the transmitter's optics prefers to be small value for a high transmitting efficiency. Fig. 13(b) shows the polarization-dependent loss as a function of f-number. The polarization-dependent loss exhibited low values regardless of the f-number.

As mentioned above, PSGCs for the optical antenna of the LiDAR were designed and fabricated. A comparison of the simulation and experimental results indicated that there was an unexpected optical index shift caused by the fabrication error of the grating edges. The designed PSGC has many sharp edges, and they are not perfectly realized due to the linewidth of the process. To improve the receiving and transmitting efficiency, it is necessary to modify the design of the PSGC, that is, rounding the sharp edges at the simulation model step, adjusting the depth of the grating, and so on to reduce the fine reflection component. The excess loss from the non-vertical diffracted light is also expected to reduce.

5. Conclusion

We designed GCs for the optical antenna based on the FDTD simulation, then demonstrated that the fabricated VGCs couple the light in a perfectly vertical direction with respect to the chip, as simulated. Subsequently, the PSGCs were designed by modifying the VGCs. We achieved the transmission of polarization-multiplexed light in a vertical direction with respect to the chip using the fabricated PSGCs. The transmitting and receiving efficiencies of the PSGCs were calculated, and then the optical parameter for maximizing them was clarified. It is expected that the polarization-dependent loss of the PIC-based LiDAR can be decreased using the PSGCs as the optical antenna. However, the PIC-based LiDAR with the designed PSGCs would have a low detection efficiency yet because it is proportional to the product of $\eta_{tP,\ tS}$ and $\eta_{rP,\ rS}$. For example, it is expected to optimize the detection efficiency by making the NFP wider and the FFP narrower. These are expected to be achieved by optimization of the chirped section's design, the etching depth, and so on.

This technology requires no additional post-processing or any changes in the foundry process. Additionally, it can decrease the packaging cost because of the ease of alignment. Accordingly, it is expected to accelerate the study of optical integrated circuits-based LiDAR and other optical applications.

Disclosures: The authors declare no conflicts of interest.

Acknowledgment

The authors acknowledge Advanced Micro Foundry Pte. Ltd., Singapore.

References

[1] R. H. Rasshofer, and K. Gresser, "Automotive radar and lidar systems for next generation driver assistance functions," *Adv. Radio Sci.*, vol. 3, pp. 205–209, 2005.

[2] J. Sun, E. Timurdogan, A. Yaacobi, E. S. Hosseini, and M. R. Watts, "Large-scale nanophotonic phased array," *Nature*, vol. 493, pp. 195–199, 2013.

[3] H. Abediasl, and H. Hashemi, "Monolithic optical phased-array transceiver in a standard SOI CMOS process," *Opt. Exp.*, vol. 23, no. 5, pp. 6509–6519, 2015.

[4] D. Inoue, T. Ichikawa, A. Kawasaki, and T. Yamashita, "Demonstration of a new optical scanner using silicon photonics integrated circuit," *Opt. Exp.*, vol. 27, no. 3, pp. 2499–2508, 2019.

[5] J. Yang, Z. Zhou, H. Jia, X. Zhang, and S. Qin, "High-performance and compact binary blazed grating coupler based on an asymmetric subgrating structure and vertical coupling," *Opt. Lett.*, vol. 36, pp. 2614–2617, 2011.

[6] Y. Ding, C. Peucheret, H. Ou, and K. Yvind, "Fully etched apodized grating coupler on the SOI platform with -0.58 dB coupling efficiency," *Opt. Lett.*, vol. 39, pp. 5348–5350, 2014.

[7] Y. Li, L. Li, B. Tian, G. Roelkens, and R. G. Baets, "Reflectionless tilted grating couplers with improved coupling efficiency based on a silicon overlay," *IEEE Photon. Technol. Lett.*, vol. 25, no. 13, pp. 1195–1198, Jul. 2013.

[8] R. Marchetti, C. Lacava, L. Carroll, K. Gradkowski, and P. Minzioni, "Coupling strategies for silicon photonics integrated chips," *Photon. Res.*, vol. 7, no. 2, pp. 201–239, 2019.

[9] C. A. Alonso-Ramos *et al.*, "High-directionality L-shaped fiber-chip grating couplers realized in 300-mm silicon-on-insulator platform with deep-ultraviolet lithography," in *Proc. SPIE 10535, Integr. Opt.: Devices, Mater., Technol. XXII*, 2018, 105350W.

[10] F. Van Laere *et al.*, "Compact focusing grating couplers for silicon-on-insulator integrated circuits," *IEEE Photon. Technol. Lett.*, vol. 19, pp. 1919–1921, Dec. 2007.

[11] X. Chen, and H. K. Tsang, "Polarization-independent grating couplers for silicon-on-insulator nanophotonic waveguides," *Opt. Lett.*, vol. 36, no. 6, pp. 796–798, 2011.

[12] W. S. Zaoui, A. Kunze, W. Vogel, and M. Berroth, "CMOS-compatible polarization splitting grating couplers with a backside metal mirror," *IEEE Photon. Technol. Lett.*, vol. 25, no. 14, pp. 1395–1397, Jul. 2013.

[13] Z. Zhang *et al.*, "Two-dimensional apodized grating coupler for polarization-independent and surface-normal optical coupling," *J. Lightw. Technol.*, vol. 38, no. 15, pp. 4037–4044, 2020.

[14] A. Mekis *et al.*, "A grating-coupler-enabled CMOS photonics platform," *IEEE J. Sel. Topics Quant. Electron.*, vol. 17, no. 3, pp. 597–608, May/Jun. 2011.

[15] B. Chen *et al.*, "Two-dimensional grating coupler on silicon with a high coupling efficiency and a low polarization-dependent loss," *Opt. Exp.*, vol. 28, pp. 4001–4009, 2020.

[16] D. Taillaert, P. Bienstman, and R. Baets, "Compact efficient broadband grating coupler for silicon-on-insulator waveguides," *Opt. Lett.*, vol. 29, vol. no. 23, pp. 2749–2751, 2004.

[17] X. Chen, C. Li, and H. K. Tsang, "Fabrication-tolerant waveguide chirped grating coupler for coupling to a perfectly vertical optical fiber," *IEEE Photon. Technol. Lett.*, vol. 20, no. 23, pp. 1914–1916, Dec. 2008.

[18] Z. Zhang *et al.*, "High-efficiency apodized bidirectional grating coupler for perfectly vertical coupling," *Opt. Lett.*, vol. 44, no. 20, pp. 5081–5084, 2019.

[19] Y. Tong, W. Zhou, and H. K. Tsang, "Efficient perfectly vertical grating coupler for multi-core fibers fabricated with 193 nm DUV lithography," *Opt. Lett.*, vol. 43, no. 23, pp. 5709–5712, 2018.